CLIMATOLOGY

Skillful multiyear prediction of flood frequency along the US Northeast Coast using a high-resolution modeling system

Liping Zhang[1,2]*, Thomas L. Delworth[1], Vimal Koul[3], Andrew Ross[1], Charles Stock[1], Xiaosong Yang[1], Fanrong Zeng[1], Andrew Wittenberg[1], Jian Zhao[4], Qinxue Gu[3], Shouwei Li[3]

Using tide gauge (TG) observations, we identify pronounced multidecadal fluctuations in sea level along the US Northeast Coast (USNEC) superimposed on a long-term increasing trend. This multidecadal sea level variability, largely arising from fluctuations in the buoyancy-driven Atlantic meridional overturning circulation (AMOC), substantially modulates the frequency of flood occurrences along the USNEC and serves as a source of multiyear predictability. Using an initialized dynamical downscaling decadal prediction system with a $^{1}/_{12}$° ocean resolution, we demonstrate that flood frequency along the USNEC can be predicted on multiyear to decadal timescales. The long-term increasing trend in flood frequency, mainly driven by increasing greenhouse gases and associated radiative forcing changes, can be predicted a decade ahead. Furthermore, detrended flood frequency along the USNEC exhibits prediction skill for up to 3 years, as verified by TG observation. This multiyear prediction skill is achieved using prediction models that are initialized from our best estimate of observed AMOC.

INTRODUCTION

Sea level rise (SLR) poses one of the most pressing and societally relevant challenges, as the climate continues to warm (*1*–*9*). While the global mean sea level is rising, regional sea level changes are distributed unevenly, with certain regions experiencing faster rates of rise than the global average (*10*–*15*). The US Northeast Coast (USNEC) has been identified as a hotspot for accelerated SLR over the North Atlantic (NA) Ocean in most recent decades (*12*–*15*). The weakening of Atlantic meridional overturning circulation (AMOC) due to global warming has been proposed as a primary cause for the rapid SLR along the USNEC in future climates (*12*, *15*). However, the contribution of present-day AMOC variations, influenced by both external forcing and internal variability (*16*, *17*), to sea level variability along the USNEC remains unclear.

The USNEC is particularly vulnerable to sea level changes due to its high population density and the resulting socioeconomic consequences (*15*, *18*). In comparison to other US coastal regions, such as the Gulf Coast or the West Coast, sea level variations along the USNEC tend to be more influenced by the interaction between large-scale oceanic currents (such as the Gulf Stream and AMOC) and local features. The timescale can range from short-term variations due to storms, waves, or tides to long-term changes driven by climate factors and ocean circulation shifts (*7*, *14*, *15*, *18*–*21*). Long-term SLR and low-frequency sea level variabilities establish a background state that modulates the short-term water levels (*22*). Coastal flooding typically occurs because of synoptic weather events (*14*) and is often compounded by high tide and decadal to centennial SLR. In tide gauge (TG) observations, the detrended sea level time series along the USNEC display a notable multidecadal variation (Fig. 1A and fig. S1) (*23*, *24*), very likely stemming from the AMOC signal. The multidecadal increase in background sea level is anticipated to markedly increase the risk of coastal flooding, particularly when they coincide with storms, hurricanes, ocean waves, or high tides. Furthermore, the AMOC not only has the potential to influence background sea level state but may also affect storms and the associated storm surges, thereby further amplifying the risk of coastal flooding (*25*).

Flooding along the USNEC has the potential to reshape the coastal environment by displacing barrier islands and damaging habitats crucial for supporting wildlife (*8*, *9*). Moreover, it poses threats to both lives and infrastructure in coastal regions, resulting in population relocation (*1*–*3*, *23*). Hence, there is an urgent necessity to understand and forecast the frequency of flood occurrences along the USNEC to aid in mitigating and adapting to the impacts of flooding. In this study, we combine the Geophysical Fluid Dynamics Laboratory (GFDL) global decadal prediction system using a coarse resolution ocean model (*26*, *27*) with a regional high ocean resolution ($^{1}/_{12}$°) model (*28*, *29*) to provide regionally refined predictions of the frequency of flood occurrences along the USNEC. We demonstrate that the multidecadal sea level variations along the USNEC in observations are largely influenced by buoyancy-driven fluctuations in the AMOC. These AMOC multidecadal variations have the potential to modulate the frequency of flood occurrences and substantially increase flood risk along the USNEC after 2005. Using a dynamically downscaled decadal prediction system (*28*, *29*), we find that, in addition to a predictable response to the climate change–driven SLR trend, variations in flood frequency along the USNEC associated with the AMOC can be predicted up to 3 years in advance.

RESULTS

AMOC-driven multidecadal sea level variations along the USNEC

To explore the potential role of AMOC in the observed multidecadal sea level variations along the USNEC, we use two GFDL reanalyses: the Seamless system for Prediction and Earth system Research

[1]NOAA/Geophysical Fluid Dynamics Laboratory, Princeton, NJ, USA. [2]University Corporation for Atmospheric Research, Boulder, CO, USA. [3]Atmospheric and Oceanic Science, Princeton University, Princeton, NJ, USA. [4]Horn Point Laboratory, University of Maryland Center for Environmental Science, Cambridge, MD, USA.
*Corresponding author. Email: Liping.Zhang@noaa.gov

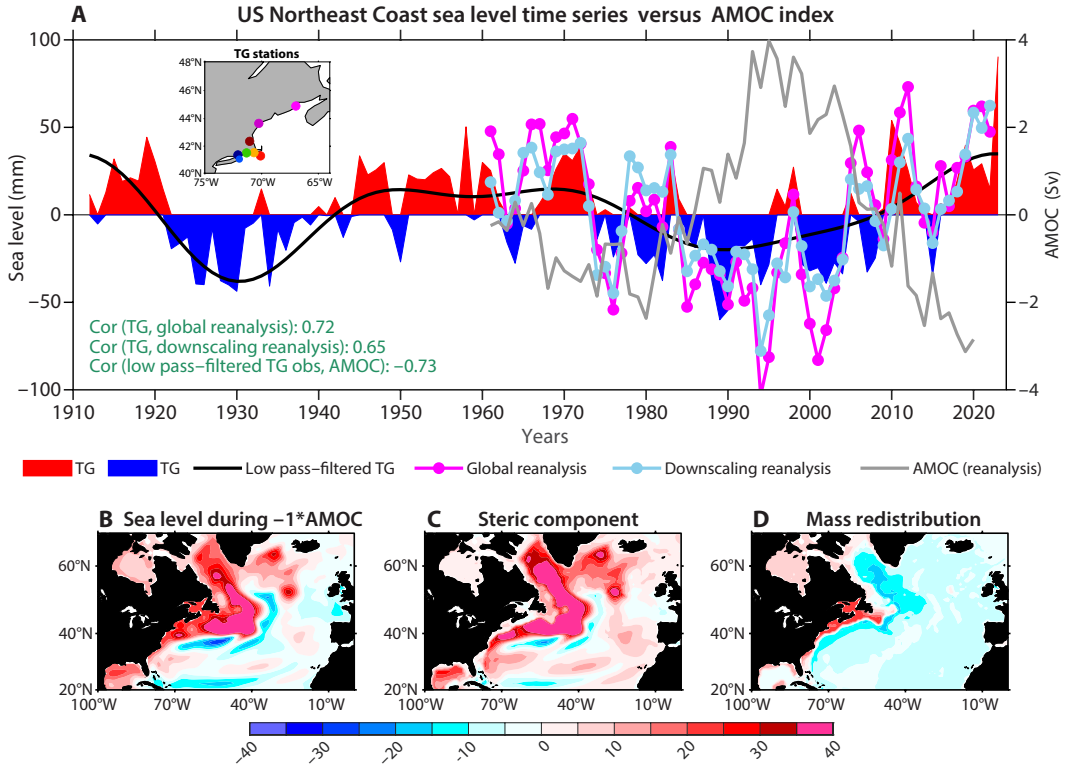

Fig. 1. Multidecadal sea level variations along the USNEC in observation and GFDL reanalyses. (**A**) Time series of the detrended annual mean sea level anomalies composited along the USNEC in TG observation (red and blue shadings), Geophysical Fluid Dynamics Laboratory (GFDL) Seamless system for Prediction and Earth system Research (SPEAR) global reanalysis (magenta line), and dynamical downscaling reanalysis (light blue line), along with the anomalous AMOC index in SPEAR global reanalysis (gray line). Units are millimeters and sverdrup for the sea level and AMOC index, respectively. The black line denotes the 15-year low pass–filtered sea level time series in TG observations. The AMOC index is defined as the maximum value of the Atlantic stream function below 500 m within the 20°N to 60°N latitude band in-depth space. An inset plot in (A) shows the TG locations along the USNEC. obs, observation; Cor, correlation. (**B**) Regression of the annual mean sea level anomalies over the NA Ocean against the normalized AMOC index in global reanalysis, multiplied by a factor of −1. The unit is millimeters. (**C**) Same as (B) but for the steric sea level component. (**D**) Same as (B) but for the mass redistribution component.

(SPEAR) global reanalysis with a 1° ocean resolution (*27*) and a dynamically downscaled reanalysis with a $^{1}/_{12}$° ocean resolution (*28*). Both datasets are partially constrained by atmospheric and sea surface temperature (SST) observations (see Materials and Methods). In Fig. 1A, we display the detrended annual mean sea level time series composited along the USNEC in TG observations and two reanalyses, alongside the AMOC index in global reanalysis. The sea level anomalies in TG observations exhibit pronounced multidecadal variability (Fig. 1A and fig. S1), with elevated sea levels before 1920, during 1945–1980, and after 2005, and decreased sea levels during 1920–1940 and 1975–2005. Both the global and downscaled reanalyses effectively capture the observed multidecadal sea level variations, with correlations of 0.72 and 0.65 ($P < 0.01$) with TG observations, respectively. Sea levels at TG stations are anticorrelated with the AMOC index in global reanalysis, with a correlation of −0.73 ($P < 0.01$). We further demonstrate in fig. S2 that this multidecadal sea level variability extends beyond coastal regions, encompassing the entire NA basin (fig. S2A). The empirical orthogonal function (EOF) analysis of detrended NA sea level in global reanalysis reveals that the first principal component (PC1) fluctuates on multidecadal timescales, aligning in phase with the low pass–filtered TG sea level observations and out of phase with the AMOC index (fig. S2B). These phenomena imply that the multidecadal variations in sea level over the NA Ocean and USNEC are closely linked to multidecadal fluctuations in the AMOC.

To verify this hypothesis, we conduct a regression analysis of NA sea level in global reanalysis against the AMOC index (Fig. 1B). We observe comma-shaped sea level anomalies in the western Atlantic, characterized by elevated sea levels in the western subpolar ocean during a negative AMOC phase and with a maximum east of Newfoundland extending southwestward to the USNEC (Fig. 1B), and, conversely, reduced sea levels during a positive AMOC phase. This sea level pattern shares great similarities with the EOF1 spatial pattern of NA sea level in the reanalysis (fig. S2A), suggesting that the AMOC serves as a driver of multidecadal sea level fluctuations over the NA. This sea level pattern also closely resembles the sea level changes projected in future climate scenarios due to forced AMOC weakening (*15*), indicating that the AMOC has the potential to affect the USNEC sea level in both current and future climates. We further decompose the AMOC-associated dynamic sea level anomalies (Fig. 1B) into contributions from the steric sea level component (Fig. 1C), which results from density changes, and the mass redistribution component (Fig. 1D), which arises from bottom pressure changes. The elevated sea levels along the USNEC during the AMOC negative phase are largely attributed to the mass redistribution term (Fig. 1D), driven by the horizontal gradient of steric SLR

between the interior ocean and the coastal region (Fig. 1C). During the negative phase of AMOC, the weakening of deep-water formation and its associated southward propagation induce warming in the deep ocean, resulting in steric SLR along the path of the deep western boundary current. Conversely, steric SLR is very small along coastal regions due to its shallow depth. This steep steric SLR gradient across the shelf break ultimately leads to increased mass loadings along the USNEC (*15*, *30*), consequently causing high sea levels in that area. The opposite occurs during the positive phase of AMOC.

Past work has shown that the simulated multidecadal variations of the AMOC can be driven by the observed multidecadal fluctuations of the NA Oscillation (NAO) (*31*). During the positive phase of NAO, cold and dry air from the North American continent is transported over the warm oceans, resulting in increased heat flux loss from the ocean to the atmosphere in the Labrador Sea and the subpolar region of NA. This process enhances deep-water formation, consequently strengthening the AMOC, and vice versa during the negative phase of NAO (*31*, *32*). Through a sensitivity experiment with realistic additional NAO flux anomalies (fig. S3) (*31*), we observe that the observed multidecadal NAO variability drives multidecadal AMOC variations. This, in turn, induces multidecadal sea level variations along the USNEC through steric sea level anomalies and the resulting mass redistribution processes. In this sensitivity run, multidecadal sea level variations along the USNEC show high correlations with both TG sea level observations and the NAO-driven AMOC index in the model, yielding correlation coefficients of 0.67 and −0.77 ($P < 0.01$), respectively.

Modulation effect of the AMOC on the flood frequency along the USNEC

The multidecadal AMOC fluctuations drive multidecadal sea level variations along the USNEC, which further modulate the frequency of coastal flood occurrences. In Fig. 2 (A to H), we present the annual expected exceedances for daily maximum water levels in 2005–2022 relative to the 1983–2001 mean higher high water (MHHW) tidal datum at eight TG stations along the USNEC (see Materials and Methods), using observations and two GFDL reanalyses. The dark red lines in Fig. 2 (A to H) represent the minor flood threshold specified in the National Oceanic and Atmospheric Administration (NOAA) technical report (*33*), indicating flooding when the daily maximum water level surpasses this threshold. To assess the impact of linear trend and AMOC on the number of exceedances, we calculate annual exceedances after removing these processes from water level records (see Materials and Methods). Overall, both GFDL reanalyses reasonably capture the distributions of exceedances, although they generally exhibit smaller magnitudes than observed at most stations. This outcome is expected, as our models have relatively low atmosphere resolution and do not incorporate certain real-world processes such as land ice melting and vertical land movement (*27*, *28*). At most TG stations, the downscaled reanalysis outperforms the global reanalysis, largely due to its higher ocean resolution and inclusion of explicit tides (*29*).

As expected, the strongest influence on the increasing flood frequency is the linear SLR trend, primarily reflecting the role of greenhouse gas warming and land subsidence. The removal of this linear trend from sea level records results in a reduction of annual exceedances by more than twofold at all stations (black versus magenta lines in Fig. 2, A to H). While the influence of AMOC is of secondary importance, it remains substantial. Eliminating the multidecadal fluctuations of AMOC from the USNEC would decrease the number of exceedances during 2005–2022 by ~20 to 50% across different TG stations (black versus blue lines in Fig. 2, A to H). The reliability of multidecadal AMOC fluctuations in reanalysis also introduces some uncertainties in this range. However, because there are no direct multidecadal observations of AMOC, using the AMOC signal from the reanalysis remains our best available option. We further show in Fig. 3 the temporal variation in observed flood days and the changes in flood days after subtracting the linear trend and AMOC-related influence from TG observations (see Materials and Methods). Because of global warming and land subsidence, the number of flood days per year has been steadily increasing (*22*), with a notable acceleration after 2005 (Fig. 3, A and C, and figs. S4 and S5). Besides the SLR trend, AMOC fluctuations amplify flood risk post-2005 along the USNEC, particularly north of the Boston station (Fig. 3B and figs. S4 and S5). The AMOC-related sea level changes contribute up to eight flood days per year post-2005 along the USNEC in observation, comprising ~20 to 50% of the total flooding events across different TG stations (Fig. 3, A and B). This modulation effect of AMOC on coastal flooding is also evident in GFDL reanalyses post-2005, albeit with some underestimation (overestimation) of flood risk north (south) of Boston (figs. S4 and S5). This discrepancy could arise from the reanalyses potentially exaggerating or reducing AMOC variability and its impact in certain areas or from differences in flood sensitivity to AMOC changes between the model and the observations. In contrast, the AMOC mitigated the number of floods during 1980–2005, acting in opposition to the SLR trend (Fig. 3, B and C). Before 1980, the AMOC increased the flood risk, thus positively reinforcing the long-term SLR trend (Fig. 3, B and C). The modulation effect of AMOC on flooding risk, characterized by its up and down fluctuations, aligns with the mean sea level characteristics associated with AMOC fluctuations in reanalysis (Fig. 1A and fig. S2B). Here, the influence of tides on the number of flood days is illustrated by comparing Fig. 3A with figs. S4A and S5A. At the Eastport station (the first row in each subplot), flood day peaks are observed in 1979, 1998, and 2016 in TG observation (Fig. 3A), which coincide with peaks in the 18.6-year nodal modulation of tidal amplitude (*34*). Similar flood peaks appear in the dynamically downscaled reanalysis due to the explicit inclusion of tides (fig. S5A), but these peaks are absent in the SPEAR global reanalysis (fig. S4A), which lacks tide simulation.

The modulation effect of AMOC on coastal floods is further supported by the SPEAR control simulation (see Materials and Methods). In Fig. 2I, the annual exceedance for daily mean water levels relative to the long-term mean water levels is depicted along the USNEC during different phases of AMOC in the control run. The number of exceedances during the AMOC negative phase is more than that during the AMOC positive phase. The probability density functions for the annual occurrence of extreme sea level (ESL) (see Materials and Methods) along the USNEC during the AMOC negative phase shift toward higher occurrences of ESL, consequently increasing the probability of coastal flooding (Fig. 2J). The mean sea level background along the USNEC is high during the negative phase of AMOC largely due to the mass redistribution term (fig. S6). These higher-than-normal background sea levels are more favorable to produce ESLs compared to the AMOC positive phase, thus substantially increasing flood risk along the USNEC.

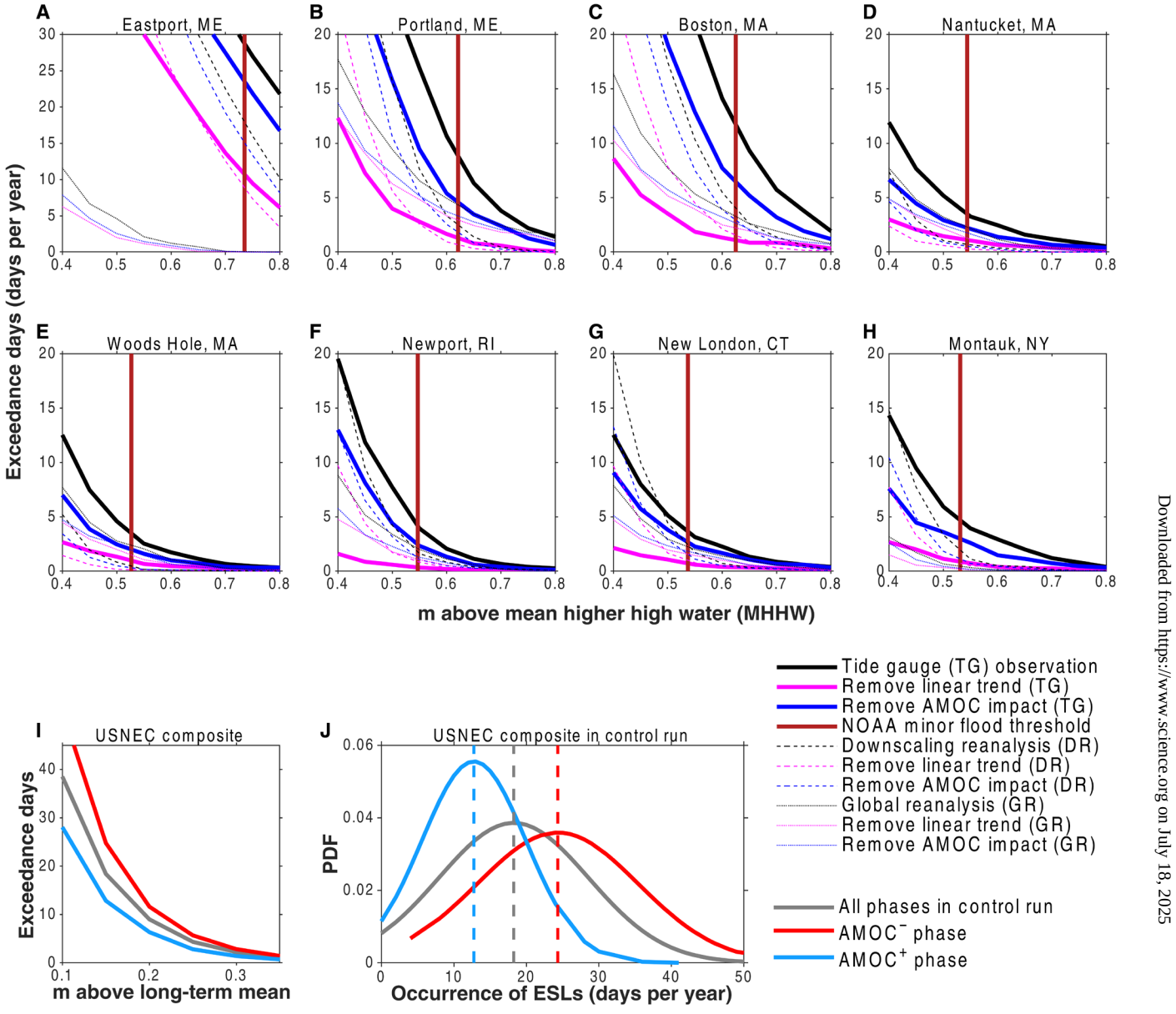

Fig. 2. Modulation effect of the linear trend and AMOC on the USNEC flood risk. (**A** to **H**) Annual exceedances of daily maximum water levels averaged in 2005–2022 with respect to 1983–2001 MHHW tidal datum at Eastport (A), Portland (B), Boston (C), Nantucket (D), Woods Hole (E), Newport (F), New London (G), and Montauk (H) stations along the USNEC in TG observation (solid lines), dynamical downscaling reanalysis (dashed lines), and SPEAR global reanalysis (dotted lines). The black lines denote the total water level records, the blue lines denote the records with the removal of AMOC-related sea level, and the magenta lines denote the records with the linear trend subtracted. The dark red lines in (A) to (H) denote the NOAA minor flood thresholds specified in the NOAA technical report. (**I**) Annual exceedance for daily mean water levels respective to the long-term mean daily mean water levels composited along the USNEC during the AMOC positive phase (baby blue line), the AMOC negative phase (red line), and all phases (gray line) in SPEAR_HI control simulation. (**J**) Probability density functions (PDFs) for the extreme sea level (ESL) occurrence frequency composited along the USNEC during different phases of AMOC in SPEAR_HI control simulation. The day of ESL occurrence is defined as the day when the daily water level exceeds the 95th percentile threshold of the daily water level distribution across all days and years in the control run. The AMOC index is defined as the maximum value of the Atlantic stream function below 500 m within the 20°N to 60°N latitude band. Positive (negative) phases of the AMOC are identified when the AMOC index exceeds (falls below) 1 SD from the mean. Unit is days per year for the annual exceedances and ESL occurrence frequency.

Multiyear to decadal predictability of flood frequency along the USNEC

In this section, we aim to explore whether the predictable AMOC (*35*–*37*) could serve as a source of multiyear to decadal predictability for the frequency of coastal flood occurrences. First, we use a diagnostic method called average predictability time (APT) (*38*–*40*) to assess the perfect model predictability of the frequency of ESL occurrence (number of days exceeding the 95th percentile in a year; see Materials and Methods) over the NA Ocean in the SPEAR control simulation. The APT analysis resembles EOF decomposition but focuses on decomposing predictability rather than variance. We show in Fig. 4 (A and B) the leading predictable component of the

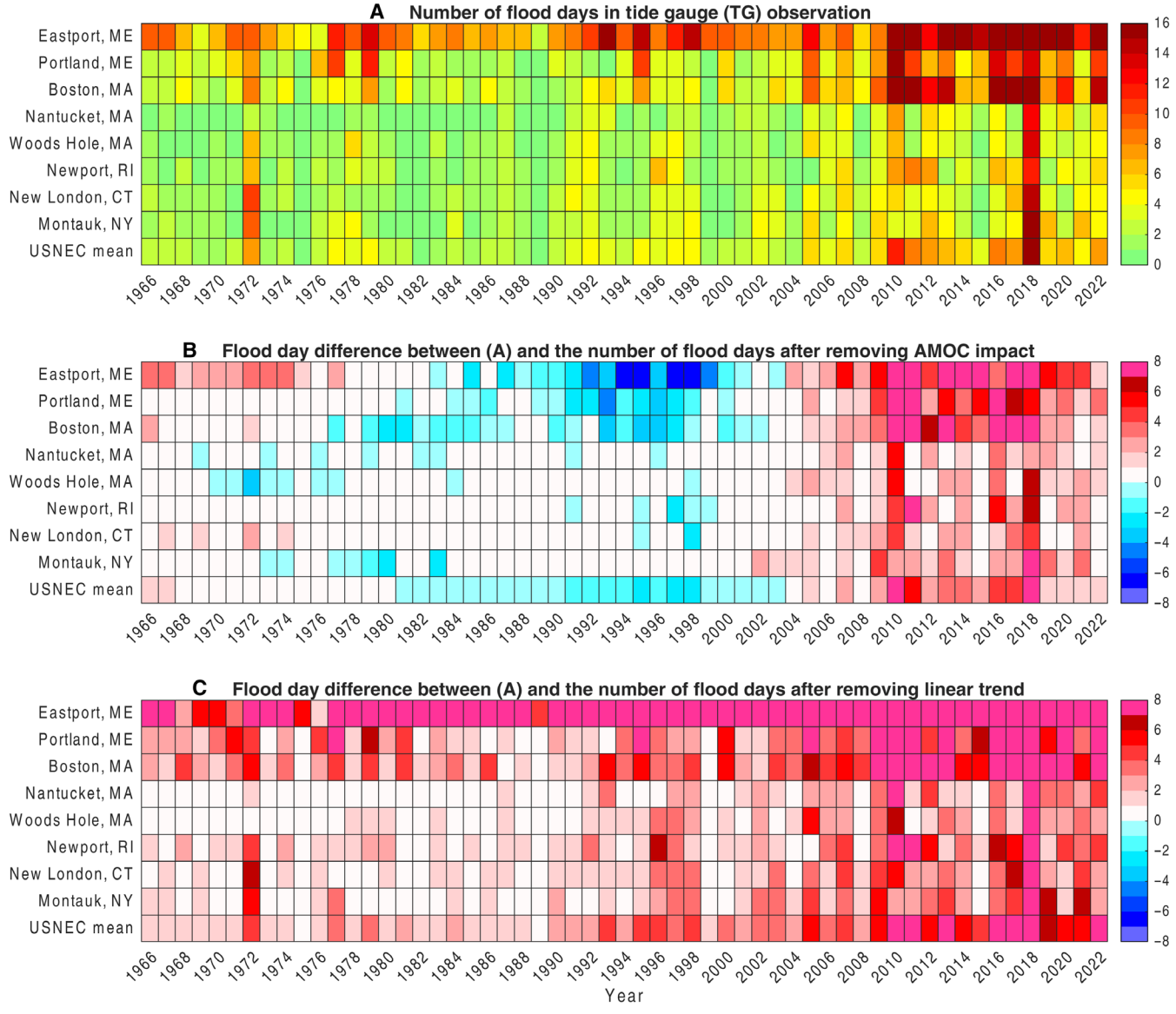

Fig. 3. Influence of the AMOC and linear trend on the USNEC flood days in TG observations. (**A**) The number of flood days (days per year) at each TG station along the USNEC as a function of time. A day is identified as a flood day when hourly water levels exceed the minor flood threshold at least once within a 24-hour period. (**B**) Flood day difference between the total number of flood days [denoted in (A)] and the number of flood days after removing the AMOC-related sea level from water level records. (**C**) Same as (B) but for the flood day difference between the total number of flood days and the number of flood days after removing the linear trend from water level records. The last row in each subplot shows the average number of flood days for eight TG stations along the USNEC.

ESL occurrence frequency over the NA Ocean. The most predictable component (APT1) has large loadings over the western subpolar ocean, peaking east of Newfoundland and extending toward the USNEC. When we apply the APT analysis to a smaller region to zoom into the Northwest Atlantic (NWA) Ocean, similar results are obtained (Fig. 4, C and D). The squared multiple correlation R^2 indicates that this component has a predictability of up to 7 years (Fig. 4, B and D). This APT1 spatial pattern shares great similarities with the annual mean sea level pattern associated with the AMOC fluctuations (Fig. 1B) and also resembles the most predictable annual mean sea level pattern over the NA in previous work (*24*). These similarities suggest a strong connection between the multiyear predictability of ESL occurrence frequency over the NA and the background sea level predictability, both of which are attributable to multidecadal AMOC variations. Figure 4E shows the lagged regressions of the Atlantic stream function against the NA APT1 time series. At a lag of 0 years, the APT1 component corresponds to a peak negative phase of the AMOC. The lagged regressions (−16 to 16 years) reveal a clear evolution of the AMOC cycle. Analyses from the control run suggest that if we could accurately initialize the AMOC in a decadal prediction model, then the future forecast of flood frequency along the USNEC is potentially predictable on multiyear timescales.

We then investigate whether the flood frequency predictability described above can be translated to actual prediction skill in the GFDL initialized dynamically downscaled decadal prediction system

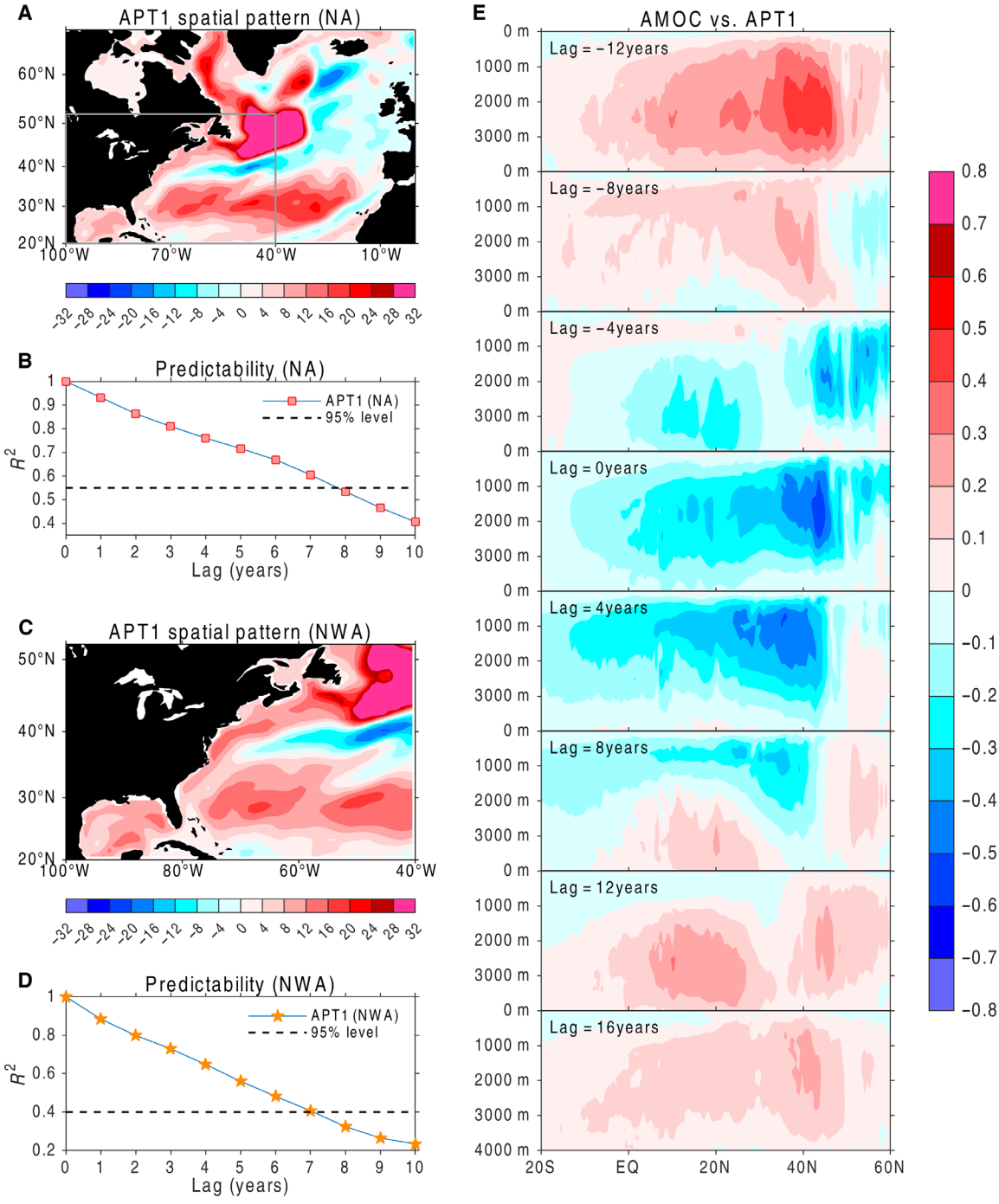

Fig. 4. The multiyear predictability of ESL occurrence frequency in the SPEAR control simulation. (**A**) Spatial pattern of the leading predictable (APT1) ESL occurrence frequency (days per year) over the NA Ocean in SPEAR_HI control simulation diagnosed from the APT method. The gray box in (A) denotes the small NWA region. (**B**) Perfect model predictability of the APT1 component, quantified by the squared multiple correlation coefficient R^2. The dashed black line denotes the 95% confidence level estimated by Monte Carlo experiments. (**C** and **D**) Same as (A) and (B) but for the small NWA region. (**E**) Lagged regressions (−12 to 16 years) of AMOC stream function against the NA APT1 time series. Negative (positive) lags indicate that the AMOC leads (lags) the APT1 time series. Unit is sverdrup.

(*28*) (see Materials and Methods). Figure 5 (A to F) displays the most predictable components of ESL occurrence frequency in the decadal hindcasts and their associated prediction skills. The APT1 component shows an upward trend, with widespread increases in the frequency of ESL occurrences in the NWA Ocean except over the Gulf Stream extension region (Fig. 5, A, C, and E). This component primarily reflects the influence of external forcing, as demonstrated by the similarity between the hindcast time series and the externally forced time series (yellow line in Fig. 5C), where the external forcing is derived by projecting the ensemble mean of large ensemble historical simulations onto the APT1 spatial pattern. This component exhibits prediction skill for a decade, verified by satellite observations (Fig. 5E). We note that the APT1 component strongly imprints on the USNEC (Fig. 5A), indicating an increasing frequency of coastal floods, which is predictable on decadal timescales (Fig. 5, G and I). The flood frequency along the USNEC in hindcasts at different lead years closely correlates with that in reanalysis and TG observations (Fig. 5G), predicting a decade in advance when verified by both reanalysis and TG observation (Fig. 5I).

The second most predictable component of the frequency of ESL occurrence in the downscaled hindcasts (APT2) exhibits a peak to the east of Newfoundland that extends to the US East Coast (Fig. 5B).

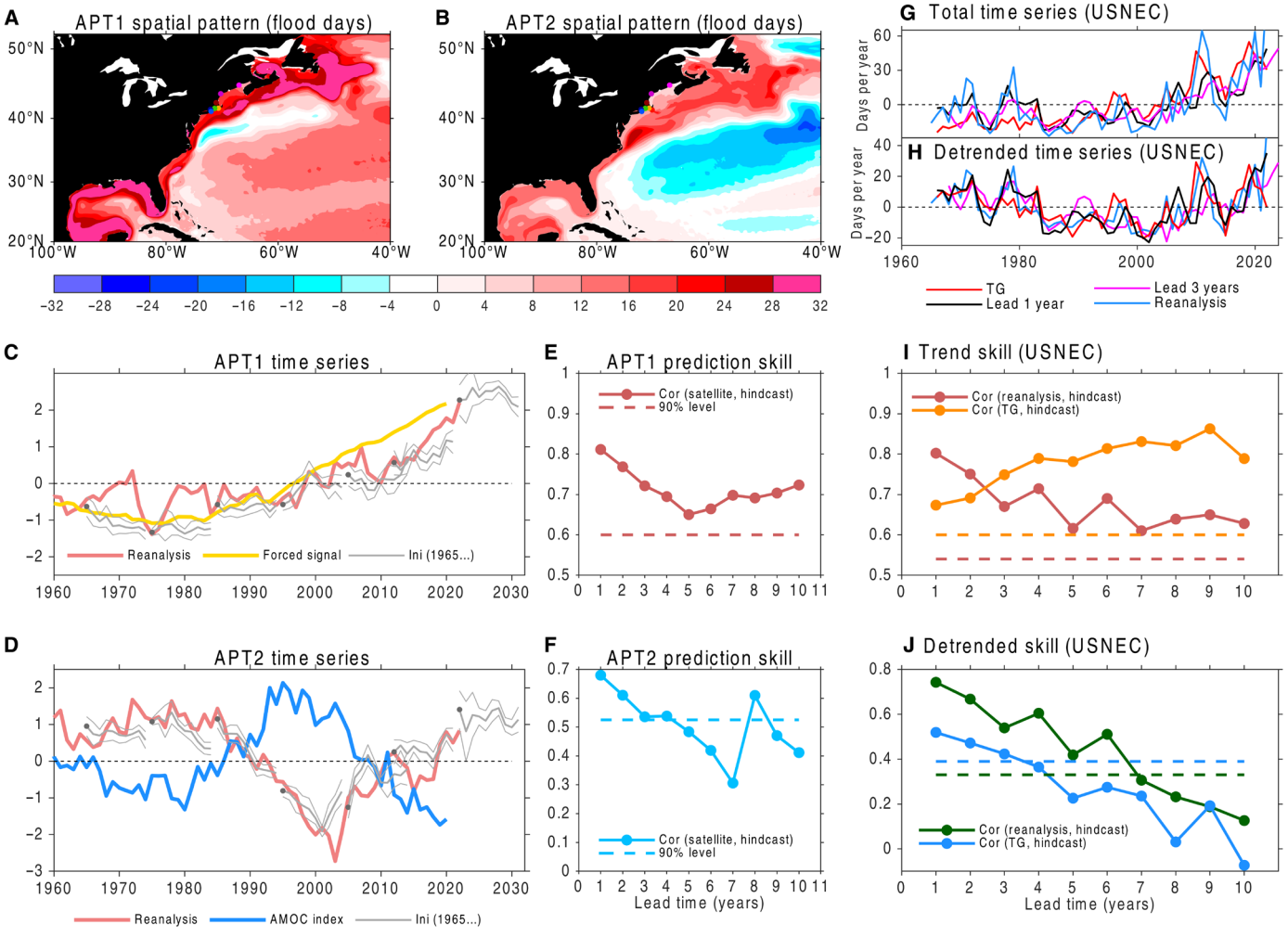

Fig. 5. The multiyear to decadal prediction skill of the frequency of ESL or flood occurrences in the downscaled decadal hindcasts. (**A**) Spatial pattern of the leading predictable ESL occurrence frequency (days per year) (APT1) obtained from the APT method. (**B**) Spatial pattern of the secondary most predictable component (APT2). (**C**) The APT1 (ensemble mean, thick gray line; ensemble spread, two thin gray lines) time series as a function of lead times in the hindcasts initialized (Ini) from 1965 to 2022. The red line is the time series for projecting the downscaled reanalysis onto the APT1 spatial pattern. The yellow line is the time series for projecting the ensemble mean of large ensemble historical simulations onto the APT1 spatial pattern, representing the external forcing. (**D**) Same as (C) but for the APT2 time series. The baby blue line denotes the AMOC index in global reanalysis (maximum stream function within 20°N to 60°N and below 500 m). (**E**) The prediction skill of the APT1 component, estimated by correlations (Cor) between the APT1 time series in hindcasts and the projected satellite observation time series, where the satellite time series is obtained by projecting the satellite observation onto the APT1 spatial pattern. (**F**) Same as (E) but for the APT2 time series. (**G**) Time series of the total flood days composited along the USNEC [color dots in (A)] in TG observation (red line), downscaled reanalysis (blue line), and hindcasts at leads of 1 and 3 years (black and magenta lines). (**H**) Same as (G) but for the linear detrended flood days. (**I**) Anomaly correlation between the total flood days in TG observation (orange line) and downscaled reanalysis (pink line) and the flood days in initialized hindcasts as a function of lead time. (**J**) Same as (I) but for the prediction skill of linear detrended flood days. The dashed lines denote the 90% confidence level using a Monte Carlo method.

It displays pronounced multidecadal variability and varies out of phase with the AMOC index in SPEAR global reanalysis (Fig. 5D), suggesting that the APT2 component originates from the buoyancy-driven AMOC variations similar to the APT1 component of the SPEAR control simulation (Fig. 4). We find that this component can be predicted up to ~4 years in advance when verified by satellite observation, although this skill is lower than the perfect model skill in control run, presumably due to initialization uncertainties, assimilation errors, and model biases (Fig. 5F versus Fig. 4, B and D). In addition, the APT2 component notably affects the USNEC. Notably, the detrended frequency of flood occurrences composited along the USNEC in TG observation shows fluctuations on multidecadal timescales, with a high risk of flooding before 1985 and after 2005 and a low risk of flooding during 1985–2005 (Fig. 5H). The detrended flood frequency along the USNEC exhibits prediction skill for up to 3 years, as verified by TG observation (Fig. 5J). This multiyear skill primarily results from successfully capturing multidecadal variability in the frequency of flood occurrences, largely driven by the AMOC. However, this skill is lower than that verified by downscaling reanalysis because of model biases, assimilation errors, and initialization uncertainties. The downscaled model ($^1/_{12}$° ocean) provides a clearer depiction of the continental shelf break and a larger amplitude of the frequency of ESL occurrences than the global SPEAR model (1° ocean) (Fig. 4, A and C, versus Fig. 5, A and B). This is probably because the higher ocean resolution better resolves the continental shelf and therefore improves the mass redistribution process.

DISCUSSION

In TG observations, we notice pronounced multidecadal fluctuations in sea levels along the USNEC. In this study, we use the GFDL modeling systems to verify that this observed multidecadal sea level variability is largely driven by the multidecadal variations in the buoyancy-driven AMOC, attributed to the observed multidecadal NAO variations. A weaker-than-normal AMOC corresponds to a higher-than-normal sea level along the USNEC and vice versa. This anticorrelated relationship between the AMOC and the sea level is only established on multidecadal timescales. On shorter timescales, sea level variabilities can be substantially influenced by other factors such as the alongshore wind, Gulf Stream position, wind-driven AMOC, and so on (*7*, *14*, *15*, *18*–*21*). On multidecadal timescales, the AMOC-induced zonal steric sea level gradient anomalies lead to mass redistributions along the USNEC, fulfilling the geostrophic balance and consequently causing sea level anomalies in that area. This mechanism operates over multidecadal timescales and aligns with the dynamics of sea level change in future climate projections (*15*).

Our study further highlights that the AMOC-influenced multidecadal sea level background state substantially affects the frequency of flood occurrences along the USNEC, providing a source of multiyear predictability. Elevated background sea levels markedly increase the risk of flooding, while low levels decrease it. Since 2005, the frequency of flood occurrences along the USNEC has been substantially influenced by the weakening of AMOC, accounting for ~20 to 50% of all flooding events across different TG stations. This contribution is substantial when compared to the influence of the global warming trend. Using an initialized decadal prediction system with a $^1/_{12}$° ocean resolution, we demonstrate the potential to predict the frequency of flood occurrences along the USNEC on multiyear timescales. The long-term increasing trend in flood frequency, largely attributed to external radiative forcing, can be predicted a decade ahead. In addition, the detrended number of floods along the USNEC exhibits prediction skill for up to 3 years, as verified by TG observation. This multiyear predictive capability primarily arises from successfully capturing multidecadal variability in the frequency of flood occurrences, predominantly influenced by the AMOC.

Our study focuses on identifying potential physical drivers and sources of predictability, rather than precisely separating the forced signal from internal variability. While the multidecadal variations in AMOC and sea level may be predominantly internally driven, they could also be partially attributed to external forcing (*41*, *42*). We also acknowledge that the GFDL model used here has relatively low atmosphere resolutions, lacks land ice components, and does not simulate climate-unrelated factors (*26*–*29*). The impacts of Greenland ice sheet melts on the AMOC and sea level are not accounted for in the model, resulting in a lower magnitude of SLR and likely degradation in the prediction skill of flood frequency. We hope future advancements in modeling and intermodel comparisons can address these and other shortcomings, thus offering more precise prediction insights for enhanced decision-making and socioeconomic management.

MATERIALS AND METHODS

Model

In our study, we use the GFDL model known as SPEAR (*26*). The ocean and ice components of SPEAR are derived from Modular Ocean Model version 6 (MOM6) (*43*), featuring 75 hybrid ocean vertical layers and ~1° horizontal resolution, with a refined $^1/_3$° meridional resolution in the tropics. The atmosphere and land components are sourced from Atmospheric and Oceanic Models version 4 (AM4-LM4) (*44*, *45*), which consists of 33 vertical levels. The low-resolution SPEAR (SPEAR_LO) has a horizontal resolution of ~100 km for the AM4-LM4, while the high-resolution SPEAR (SPEAR_HI) has a horizontal AM4-LM4 resolution of ~25 km. We conduct thousands of years of control simulation for SPEAR_LO and SPEAR_HI, with fixed radiative forcing at preindustrial 1850 concentrations. In both SPEAR control simulations, the AMOC fluctuates on multidecadal timescales, with a peak period of around 35 years (fig. S6) (*24*, *26*).

We developed a global coupled reanalysis using SPEAR_LO to initialize a retrospective global decadal prediction system (*27*). In SPEAR global reanalysis, the atmospheric temperature and winds were restored toward the 55-year Japanese Reanalysis at 6-hour intervals (*46*), while SST restoring was constrained to the Extended Reconstructed Sea Surface Temperature version 5 within 60°S to 60°N (*47*). These restorations help generate realistic air-sea boundary conditions (surface heat flux, momentum flux, and freshwater flux) in our coupled model, which, in turn, drives more accurate multidecadal AMOC variations in the reanalysis (*27*). We chose this modeling strategy to avoid the uncertainties introduced by sparse ocean observations and the potential disconnections between ocean circulation, other ocean variables, and atmospheric forcings. The high correlation of the AMOC time series at 26.5°N between the SPEAR reanalysis here and the Rapid climate change-Meridional circulation and heat flux array (RAPID array) significantly boosts our confidence in the SPEAR reanalysis (fig. S7). The SPEAR global reanalysis is then used to initialize the retrospective decadal prediction system (*27*). The decadal hindcasts are based on SPEAR_LO and consist of 10 ensemble members, each

initialized on 1 January of every year from 1961 to 2023, starting from various members of the global reanalysis. These hindcasts were integrated for 10 years, forced by realistic time-evolving radiative forcings.

We also used the MOM6_NWA12 model (*29*), a $^1/_{12}$° ocean and sea ice model specific to the NWA Ocean (260°E to 330°E, 5°N to 58°N), to downscale the SPEAR global coupled reanalysis and decadal hindcasts (*28*). This model, MOM6_NWA12, has three open boundaries, using the Flather-Orlansky radiation boundary scheme. Compared to the low-resolution global model, MOM6_NWA12 features a more realistic representation of the Gulf Stream position and coastal circulation, and it also includes tide simulation (*28*, *29*). The dynamical downscaling reanalysis based on the MOM6_NWA12 is achieved by driving the model with surface forcing and ocean boundary conditions from the SPEAR global coupled reanalysis. The global reanalysis provides daily atmospheric [sea level pressure (SLP), precipitation, temperature, and specific humidity at 2 m and winds at 10 m] and monthly oceanic [temperature, salinity, sea surface height (SSH), and velocity] data outputs, which are used as lateral boundary conditions for dynamical downscaling within the MOM6_NWA12 framework. This dynamically downscaled reanalysis comprises 10 ensemble members, each starting from 1 January 1958 and ending on 31 December 2022. To eliminate the spin-up process of the model, we discard data from the initial 7 years. We then use this dynamical downscaling reanalysis to initialize the downscaled retrospective decadal prediction system. In this prediction system, based on MOM6_NWA12, initial conditions are sourced from the dynamically downscaled reanalysis, whereas the surface atmospheric forcing and three open boundary conditions are taken from the corresponding SPEAR_LO-based global decadal hindcasts mentioned previously. The downscaled decadal hindcasts consist of 10 members, each initialized on 1 January every year from 1965 to 2022 and integrated forward for 10 years. During the analysis of the hindcast output, we minimize the systematic drift of the model by removing the lead time–dependent climatology. More detailed descriptions of the downscaled model and prediction configurations are summarized in a previous study (*28*, *29*).

Observations

We use hourly water level observations from TG stations (*48*), spanning back to the 20th century, which can be downloaded from the NOAA's National Ocean Service. In addition, we use daily gridded SSH data with a 0.25° resolution observed by satellite (*49*), obtained from the Copernicus Marine and Environment Monitoring Service. To account for land subsidence at the US TG stations, we use the vertical land movement estimates from the Glacial Isostatic Adjustment model (*50*), distributed by the Permanent Service for Mean Sea Level (PSMSL).

Flooding and ESL definitions

For the TG observations, water levels are referenced relative to the MHHW tidal datum, which represents the time mean of the higher high water height observed during each tidal day throughout the National Tidal Datum Epoch (1983–2001). As detailed in a previous study (*22*), the flooding threshold at each TG station is based on the minor flood threshold water levels specified in the NOAA technical report (*33*). The minor flood threshold refers to the stage at which flooding begins to cause some noticeable impacts, but these impacts are generally limited and not widespread. The minor flood threshold varies across different TG stations (table S1). A day is classified as a flood day when hourly water levels exceed the minor flood threshold at least once within a 24-hour period. In Fig. 2, the annual exceedances count the number of days per year when water levels exceed a specific value above the MHHW. We estimate the relative contribution of the linear trend and buoyancy-driven AMOC to the frequency of flood occurrences by counting the number of annual flood days or exceedances after subtracting each of these processes from total water level records. For example, to obtain the AMOC-related sea level fluctuations at TG stations, we regress the TG water level records onto the PC1 time series of NA sea level variability in the reanalysis (fig. S2B), which serves as a representative fingerprint of the AMOC. We acknowledge that the observation-constrained AMOC in our reanalysis could still differ from the real-world AMOC due to model biases. The reliability of multidecadal AMOC fluctuations in reanalysis may introduce some uncertainties in our calculations. However, because there are no direct multidecadal observations of AMOC, using the AMOC or AMOC fingerprint from the reanalysis remains our best available option.

In both GFDL reanalyses and initialized downscaling hindcasts, we output the daily maximum water levels. The sea level in GFDL models or reanalyses largely reflects the dynamic sea level (with a global mean of zero). The dynamic sea level in the model can be further decomposed into two components (*15*): the steric sea level, associated with density changes, and the contribution from mass redistribution, denoted by changes in bottom pressure. To align with TG observations, we incorporate the global mean steric SLR (GSSL), inverted barometer (IB) effect, and land subsidence estimates into the model. The GSSL is diagnosed from the three-dimensional density field:

$\mathrm{GSSL} = -\frac{1}{a}\int_a \int_{-h}^{\eta} \frac{1}{\rho_0}\Delta\rho dz da$, where ρ is the in situ density anomalies of seawater, $\rho_0$is the reference density of seawater, a is the surface area of the global ocean, h is the ocean depth, and η is dynamic sea level. The IB is defined as $\mathrm{IB} = -\frac{P - P_{\mathrm{gbmean}}}{\rho_0 g}$, where P is local SLP, P_{gbmean} is the global ocean–averaged SLP, ρ_0 is the seawater density, and g is the acceleration of gravity. The land subsidence is estimated from the Glacial Isostatic Adjustment model (*50*), available from the PSMSL. However, the process of land ice melting is currently not accounted for in our reanalyses, and the tide process is also absent from the SPEAR global reanalysis. These factors contribute to a smaller magnitude of water levels in GFDL reanalysis and models compared to TG observations. Given these discrepancies between the GFDL reanalysis and the TG observations, we define the frequency of floods in GFDL reanalyses based on the model's own quantities. Here, the water levels in reanalyses are referenced relative to the average of daily maximum water levels within the 1983–2001 period. At each TG station, we search for the nearest ocean point in the model and use this nearest grid as the corresponding station in reanalyses. The minor flood threshold at each station in reanalysis is defined as the 99th percentile threshold of the daily maxima water level anomaly distribution from all days and years during 1965–2022. A day is classified as a flood day when the daily maximum water level exceeds the minor flood threshold. We then count the number of flood days each year, as illustrated in Fig. 3 (B and C). Furthermore, we examined the 90th percentile and 95th percentile thresholds and observed that the lower threshold results in more flood days. Despite potential slight variations in magnitude, the conclusion drawn from Fig. 3 remains unaffected by the choice of flood threshold. In addition, we used the 99th percentile threshold to define flood days in TG observation (Fig. 5, G to J). Our analysis reveals that the annual number of flood days exceeds that reported in the NOAA technical report

mentioned earlier, indicating that the criterion used in the report is even more stringent. However, similar to our previous findings, the choice of threshold does not alter the overall conclusion of our argument.

In the SPEAR control simulation, we only output the daily mean water levels. The dynamic daily water levels are initially corrected for the IB and global steric SLR effects. Subsequently, they are referenced relative to the long-term mean daily water levels throughout the model integration period. In the control run, we use the APT method (*38*, *39*) to evaluate the perfect model predictability of water levels across the entire NA Ocean (Fig. 4). Flooding and the frequency of flood occurrences are commonly associated with coastal regions, with an emphasis on societally relevant issues. In the entire NA, we use the concept of ESL occurrence frequency throughout the paper. The day of ESL occurrence in each model grid is defined as the day when the daily water level exceeds the 95th percentile threshold of the daily water level anomaly distribution across all days and years during the entire model integration period. Here, we choose a moderate 95th percentile threshold to represent a modest extreme, which also ensures an adequate number of samples for the APT analysis. Similarly, in our analysis of initialized downscaled decadal hindcasts and satellite observations (Fig. 5), we use the moderate 95th percentile threshold to define the frequency of ESL occurrence, thereby enhancing the sample size for APT analysis and verification purposes.

APT method

The APT method (*38*, *39*) is used to identify the most predictable components of the frequency of ESL occurrences in both the SPEAR control simulation and the initialized downscaled decadal prediction system. The APT is defined as twice the integral of predictability across all lead times

$$\mathrm{APT} = 2\sum_{\tau=1}^{\infty}\left(1-\frac{\delta_{\tau}^{2}}{\delta_{\infty}^{2}}\right) \tag{1}$$

where δ_{τ}^{2} represents the ensemble forecast variance at a lead time of τ and δ_{∞}^{2} denotes climatological variance. An APT value of 1 indicates a perfect prediction, while a value of 0 suggests that the ensemble forecast variance equals the climatological variance and thus no predictability. To maximize the APT, we seek an inner product $\mathbf{q}^{T}\mathbf{x}$, where $\mathbf{q}$ is a projection vector, $\mathbf{x}$ is the state vector, and T denotes the transpose operation. Maximizing the APT leads to a generalized eigenvalue problem

$$2\sum_{\tau=0}^{\infty}\left(\sum\nolimits_{\infty}-\sum\nolimits_{\tau}\right)\mathbf{q}=\lambda\sum\nolimits_{\infty}\mathbf{q} \tag{2}$$

where λ is the eigenvalue and also represents the APT value. This makes the APT decomposition analogous to an EOF analysis, except that, here, we decompose predictability rather than variance.

When applying the APT method to control simulation or decadal hindcasts, we first extract the leading 30 PCs of the climate variables and then use these PCs to maximize the APT in Eq. 2. For the initialized decadal hindcasts, obtaining the climatological variance and forecast variance at different lead years is straightforward, given that we have 10 ensemble members and 10 years of prediction run. For the control run, however, we only have a single long ensemble member, and, thus, we adopt a linear regression model to estimate the APT as suggested by previous studies (*38*–*40*). The PCs from the control run are then split into two halves: The first half is used as training data to maximize the APT in Eq. 1, while the second half is reserved for verification. The squared multiple correlation R_{τ}^{2} is used to evaluate the potential predictability in the control run

$$R_{\tau}^{2}=\frac{\mathbf{q}^{T}\mathbf{C}_{\tau}\mathbf{C}_{0}^{-1}\mathbf{C}_{\tau}^{T}\mathbf{q}}{\mathbf{q}^{T}\mathbf{C}_{0}\mathbf{q}} \tag{3}$$

We use the training data to calculate $\mathbf{q}$ and the verification data to obtain the $\mathbf{C}_{\tau}$ and $\mathbf{C}_{0}$ two covariance terms. Last, we apply the Monte Carlo method to test the statistical significance of APT (*38*, *39*). Overall, the APT method is a more nuanced approach that integrates forecast variance, climatological variance, and lead time, providing a better understanding of where and when predictions are most reliable.

Supplementary Materials

This PDF file includes:

Figs. S1 to S7
Table S1

REFERENCES AND NOTES

1. D. M. Fitzgerald, M. S. Fenster, B. A. Argow, I. V. Buynevich, Coastal impacts due to sea-level rise. *Annu. Rev. Earth Planet. Sci.* **36**, 601–647 (2008).
2. R. J. Nicholls, P. P. Wong, V. R. Burkett, J. O. Codignotto, J. E. Hay, R. F. McLean, S. Ragoonaden, C. D. Woodroffe, "Coastal systems and low-lying areas," in *Climate Change 2007: Impacts, Adaptation and Vulnerability. Contribution of Working Group II to the Fourth Assessment Report of the Intergovernmental Panel on Climate Change,* M. L. Parry, O. F. Canziani, J. P. Palutikof, P. J. van der Linden, C. E. Hanson, Eds. (Cambridge Univ. Press, 2007), pp. 315–356.
3. R. J. Nicholls, A. Cazenave, Sea-level rise and its impact on coastal zones. *Science* **328**, 1517–1520 (2010).
4. A. Cazenave, G. L. Cozannet, Sea level rise and its coastal impacts. *Earth's Future* **2**, 15–34 (2014).
5. H. R. Moftakhari, A. Aghakouchak, B. F. Sanders, D. L. Feldman, W. Sweet, R. A. Matthew, A. Luke, Increased nuisance flooding along the coasts of the United States due to sea level rise: Past and future. *Geophys. Res. Lett.* **42**, 9846–9852 (2015).
6. G. A. Meehl, W. M. Washington, W. D. Collins, J. M. Arblaster, A. Hu, L. E. Buja, W. G. Strand, H. Teng, How much more global warming and sea level rise? *Science* **307**, 1769–1772 (2005).
7. P. B. Goddard, J. Yin, S. M. Griffies, S. Zhang, An extreme event of sea-level rise along the Northeast coast of North America in 2009–2010. *Nat. Commun.* **6**, 6346 (2015).
8. M. L. Kirwan, S. Temmerman, E. E. Skeehan, G. R. Guntenspergen, S. Fagherazzi, Overestimation of marsh vulnerability to sea level rise. *Nat. Clim. Change* **6**, 253–260 (2016).
9. M. L. Kirwan, J. P. Megonigal, Tidal wetland stability in the face of human impacts and sea-level rise. *Nature* **504**, 53–60 (2013).
10. L. Chafik, J. E. Ø. Nilsen, S. Dangerdorf, G. Reverdin, T. Frederikse, North Atlantic Ocean circulation and decadal sea level change during the altimetry era. *Sci. Rep.* **9**, 1041 (2019).
11. D. L. Volkov, S.-K. Lee, R. Dominngues, H. Zhang, M. Goes, Interannual sea level variability along the southeastern seaboard of the United States in relation to the gyre-scale heat divergence in the North Atlantic. *Geophys. Res. Lett.* **46**, 7481–7490 (2019).
12. L. Zhang, T. L. Delworth, X. Yang, F. Zeng, Q. Gu, S. Li, Causes and multiyear predictability of the rapid acceleration of U.S. Southeast Sea level rise after 2010. *npj Clim. Atmos. Sci.* **7**, 113 (2024).
13. A. H. Sallenger Jr., K. S. Doran, P. A. Howd, Hotspot of accelerated sea-level rise on the Atlantic coast of North America. *Nat. Clim. Change* **2**, 884–888 (2012).
14. T. Ezer, L. P. Atkinson, Accelerated flooding along the U.S. East Coast: On the impact of sea-level rise, tides, storms, the Gulf Stream, and the North Atlantic Oscillations. *Earth's Future* **2**, 362–382 (2014).
15. J. Yin, M. E. Schlesinger, R. J. Stouffer, Model projections of rapid sea-level rise on the northeast coast of the United States. *Nat. Geosci.* **2**, 262–266 (2009).
16. L. Zhang, C. Wang, Multidecadal North Atlantic Sea surface temperature and Atlantic meridional overturning circulation variability in CMIP5 historical simulations. *J. Geophys. Res. Oceans* **118**, 5772–5791 (2013).
17. L. Zhang, C. Wang, S.-K. Lee, Potential role of Atlantic warm pool-induced freshwater forcing in the Atlantic meridional overturning circulation: Ocean–sea ice model simulations. *Climate Dynam.* **43**, 553–574 (2014).
18. C. G. Piecuch, S. Dangendorf, G. G. Gawarkiewicz, C. M. Little, R. M. Ponte, J. Yang, How is new England coastal sea level related to the Atlantic meridional overturning circulation at 26° N? *Geophys. Res. Lett.* **46**, 5351–5360 (2019).
19. C. M. Little, C. G. Piecuch, R. M. Ponte, On the relationship between the meridional overturning circulation, alongshore wind stress, and United States East Coast sea level in the Community Earth System Model Large Ensemble. *J. Geophys. Res. Oceans* **122**, 4554–4568 (2017).

20. J. Yin, P. B. Goddard, Oceanic control of sea level rise patterns along the East Coast of the United States. *Geophys. Res. Lett.* **40**, 5514–5520 (2013).
21. C. Tebaldi, R. Ranasinghe, M. Vousdoukas, D. J. Rasmussen, B. Vega-Westhoff, E. Kirezci, R. E. Kopp, R. Sriver, L. Mentaschi, Extreme sea levels at different global warming levels. *Nat. Clim. Change* **11**, 746–751 (2021).
22. D. L. Volkov, K. Zhang, W. E. Johns, J. K. Willis, W. Hobbs, M. Goes, H. Zhang, D. Menemenlis, Atlantic meridional overturning circulation increases flood risk along the United States southeast coast. *Nat. Commun.* **14**, 5059 (2023).
23. J. Yin, Rapid decadal acceleration of sea level rise along the U.S. East and Gulf Coasts during 2010–22 and its impact on hurricane-induced storm surge. *J. Climate* **36**, 4511–4529 (2023).
24. L. Zhang, T. L. Delworth, X. Yang, F. Zeng, Skillful multiyear to decadal predictions of sea level in the North Atlantic Ocean and U.S. East Coast. *Commun. Earth Environ.* **4**, 420 (2023).
25. T. Howard, M. D. Palmer, L. C. Jackson, K. Yamazaki, Storm surge changes around the UK under a weakened Atlantic meridional overturning circulation. *Environ. Res. Commun.* **6**, 035026 (2024).
26. T. L. Delworth, W. F. Cooke, A. Adcroft, M. Bushuk, J.-H. Chen, K. A. Dunne, P. Ginoux, R. Gudgel, R. W. Hallberg, L. Harris, M. J. Harrison, N. Johnson, S. B. Kapnick, S.-J. Lin, F. Lu, S. Malyshev, P. C. Milly, H. Murakami, V. Naik, S. Pascale, D. Paynter, A. Rosati, M. D. Schwarzkopf, E. Shevliakova, S. Underwood, A. T. Wittenberg, B. Xiang, X. Yang, F. Zeng, H. Zhang, L. Zhang, M. Zhao, SPEAR: The next generation GFDL modeling system for seasonal to multidecadal prediction and projection. *J. Adv. Model. Earth Syst.* **12**, e2019MS001895 (2020).
27. X. Yang, T. L. Delworth, F. Zeng, L. Zhang, W. F. Cooke, M. J. Harrison, A. Rosati, S. D. Underwood, G. P. Compo, C. McColl, On the development of GFDL's decadal prediction system: Initialization approaches and retrospective forecast assessment. *J. Adv. Model. Earth Syst.* **13**, e2021MS002529 (2021).
28. V. Koul, A. Ross, C. Stock, L. Zhang, T. L. Delworth, A. Wittenberg, A predicted pause in the rapid warming of the Northwest Atlantic Shelf in the coming decade. *Geophys. Res. Lett.* **51**, e2024GL110946 (2024).
29. A. Ross, C. A. Stock, A. Adcroft, E. Curchitser, R. Hallberg, M. J. Harrison, K. Hedstrom, N. Zadeh, M. Alexander, W. Chen, E. J. Drenkard, H. du Pontavice, R. Dussin, F. Gomez, J. G. John, D. Kang, D. Lavoie, L. Resplandy, A. Roobaert, V. Saba, S. Shin, S. Siedlecki, J. Simkins, A high-resolution physical–biogeochemical model for marine resource applications in the Northwest Atlantic (MOM6-COBALT-NWA12 v1. 0). *Geosci. Model Dev. Discuss.* **16**, 6943–6985 (2023).
30. F. W. Landerer, J. H. Jungclaus, J. Marotzke, Ocean bottom pressure changes lead to a decreasing length-of-day in a warming climate. *Geophys. Res. Lett.* **34**, L06307 (2007).
31. T. L. Delworth, F. Zeng, G. A. Vecchi, X. Yang, L. Zhang, R. Zhang, The North Atlantic Oscillation as a driver of rapid climate change in the Northern Hemisphere. *Nat. Geosci.* **9**, 509–512 (2016).
32. T. L. Delworth, F. Zeng, The impact of the North Atlantic Oscillation on climate through its influence on the Atlantic meridional overturning circulation. *J. Climate* **29**, 941–962 (2016).
33. W. V. Sweet, B. D. Hamlington, R. E. Kopp, C. P. Weaver, P. L. Barnard, D. Bekaert, W. Brooks, M. Craghan, G. Dusek, T. Frederikse, G. Garner, A. S. Genz, J. P. Krasting, E. Larour, D. Marcy, J. J. Marra, J. Obeysekera, M. Osler, M. Pendleton, D. Roman, L. Schmied, W. Veatch, K. D. White, C. Zuzak, "Global and regional sea level rise scenarios for the United States: Updated mean projections and extreme water level probabilities along U.S. Coastlines" (NOAA Technical Report NOS 01, National Oceanic and Atmospheric Administration, 2022).
34. H. E. Baranes, J. D. Woodruff, S. A. Talke, R. E. Kopp, R. D. Ray, R. M. DeConto, Tidally driven interannual variation in extreme sea level frequencies in the Gulf of Maine. *J. Geophys. Res. Oceans* **125**, e2020JC016291 (2020).
35. X. Yang, A. Rosati, S. Zhang, T. L. Delworth, R. G. Gudgel, R. Zhang, G. Vecchi, W. Anderson, Y. Chang, T. DelSole, K. Dixon, R. Msadek, W. F. Stern, A. Wittenberg, F. Zeng, A predictable AMO-like pattern in the GFDL fully coupled ensemble initialization and decadal forecasting system. *J. Climate* **26**, 650–661 (2013).
36. R. Msadek, K. W. Dixon, T. L. Delworth, W. J. Hurlin, Assessing the predictability of the Atlantic meridional overturning circulation and associated fingerprints. *Geophys. Res. Lett.* **37**, L19608 (2010).
37. I. Polkova, D. Swingedouw, L. Hermanson, A. Köhl, D. Stammer, D. Smith, J. Kröger, I. Bethke, X. Yang, L. Zhang, D. Nicoli, P. J. Athanasiadis, M. P. Karami, K. Pankatz, H. Pohlmann, B. Wu, R. Bilbao, P. Ortega, S. Yang, R. Sospedra-Alfonso, W. Merryfield, T. Kataoka, H. Tatebe, Y. Imada, M. Ishii, R. J. Matear, Initialization shock in the ocean circulation reduces skill in decadal predictions of the North Atlantic subpolar gyre. *Frontiers in Climate* **5**, 10.3389/fclim.2023.1273770 (2023).
38. T. DelSole, M. K. Tippett, Average predictability time. Part I: Theory. *J. Atmos. Sci.* **66**, 1172–1187 (2009).
39. T. DelSole, M. K. Tippett, Average predictability time. Part II: Seamless diagnoses of predictability on multiple time scales. *J. Atmos. Sci.* **66**, 1188–1204 (2009).
40. L. Zhang, T. L. Delworth, L. Jia, Diagnosis of decadal predictability of Southern Ocean Sea surface temperature in the GFDL CM2.1 model. *J. Climate* **30**, 6309–6328 (2017).
41. J. M. Klavans, M. A. Cane, A. C. Clement, L. N. Murphy, NAO predictability from external forcing in the late 20th century. *npj Clim. Atmos. Sci.* **4**, 22 (2021).
42. F. Liu, X. Li, Y. Luo, W. Cai, J. Lu, X.-T. Zheng, S. M. Kang, H. Wang, L. Zhou, Increased Asian aerosols drive a slowdown of Atlantic meridional overturning circulation. *Nat. Commun.* **15**, 18 (2024).
43. A. Adcroft, W. Anderson, V. Balaji, C. Blanton, M. Bushuk, C. O. Dufour, J. P. Dunne, S. M. Griffies, R. Hallberg, M. J. Harrison, I. M. Held, M. F. Jansen, J. G. John, J. P. Krasting, A. R. Langenhorst, S. Legg, Z. Liang, C. McHugh, A. Radhakrishnan, B. G. Reichl, T. Rosati, B. L. Samuels, A. Shao, R. Stouffer, M. Winton, A. T. Wittenberg, B. Xiang, N. Zadeh, R. Zhang, The GFDL global ocean and sea ice model OM4.0: Model description and simulation features. *J. Adv. Model. Earth Syst.* **11**, 3167–3211 (2019).
44. M. Zhao, J.-C. Golaz, I. M. Held, H. Guo, V. Balaji, R. Benson, J.-H. Chen, X. Chen, L. J. Donner, J. P. Dunne, K. Dunne, J. Durachta, S.-M. Fan, S. M. Freidenreich, S. T. Garner, P. Ginoux, L. M. Harris, L. W. Horowitz, J. P. Krasting, A. R. Langenhorst, Z. Liang, P. Lin, S.-J. Lin, S. L. Malyshev, E. Mason, P. C. D. Milly, Y. Ming, V. Naik, F. Paulot, D. Paynter, P. Phillipps, A. Radhakrishnan, V. Ramaswamy, T. Robinson, D. Schwarzkopf, C. J. Seman, E. Shevliakova, Z. Shen, H. Shin, L. G. Silvers, J. R. Wilson, M. Winton, A. T. Wittenberg, B. Wyman, B. Xiang, The GFDL global atmosphere and land model AM4.0/LM4.0: 1. Simulation characteristics with prescribed SSTs. *J. Adv. Model. Earth Syst.* **10**, 691–734 (2018).
45. M. Zhao, J.-C. Golaz, I. M. Held, H. Guo, V. Balaji, R. Benson, J.-H. Chen, X. Chen, L. J. Donner, J. P. Dunne, K. Dunne, J. Durachta, S.-M. Fan, S. M. Freidenreich, S. T. Garner, P. Ginoux, L. M. Harris, L. W. Horowitz, J. P. Krasting, A. R. Langenhorst, Z. Liang, P. Lin, S.-J. Lin, S. L. Malyshev, E. Mason, P. C. D. Milly, Y. Ming, V. Naik, F. Paulot, D. Paynter, P. Phillipps, A. Radhakrishnan, V. Ramaswamy, T. Robinson, D. Schwarzkopf, C. J. Seman, E. Shevliakova, Z. Shen, H. Shin, L. G. Silvers, J. R. Wilson, M. Winton, A. T. Wittenberg, B. Wyman, B. Xiang, The GFDL global atmosphere and land model AM4.0/LM4.0: 2. Model description, sensitivity studies, and tuning strategies. *J. Adv. Model. Earth Syst.* **10**, 735–769 (2018).
46. S. Kobayashi, Y. Ota, Y. Harada, A. Ebita, M. Moriya, H. Onoda, K. Onogi, H. Kamahori, C. Kobayashi, H. Endo, K. Miyaoka, K. Takahashi, The JRA-55 reanalysis: General specifications and basic characteristics. *J. Meteorol. Soc. Jpn.* **93**, 5–48 (2015).
47. B. Huang, P. W. Thorne, V. F. Banzon, T. Boyer, G. Chepurin, J. H. Lawrimore, M. J. Menne, T. M. Smith, R. S. Vose, H.-M. Zhang, Extended Reconstructed Sea Surface Temperature, version 5 (ERSSTv5): Upgrades, validations, and intercomparisons. *J. Climate* **30**, 8179–8205 (2017).
48. P. Caldwell, M. Merrifield, P. Thompson, Sea level measured by tide gauges from global oceans—The Joint Archive for Sea Level holdings, version 5.5, NOAA/National Centers for Environmental Information (2015); https://doi.org/10.7289/v5v40s7w.
49. G. Taburet, A. Sanchez-Roman, M. Ballarotta, M.-I. Pujol, J.-F. Legeais, F. Fournier, Y. Faugere, G. Dibarboure, DUACS DT2018: 25 years of reprocessed sea level altimetry products. *Ocean Sci.* **15**, 1207–1224 (2019).
50. W. R. Peltier, Global glacial isostasy and the surface of the ice-age Earth: The ICE-5G (VM2) model and GRACE. *Annu. Rev. Earth Planet. Sci.* **32**, 111–149 (2004).

Acknowledgments: We thank X. Wu and J. Lou for the suggestions and comments on our paper as GFDL internal reviewers. **Funding:** This work was supported by the NOAA's Climate Program Office's Modeling, Analysis, Predictions, and Projections program, through funds from the Inflation Reduction Act Forward Looking Projections initiative grant NA23OAR4310608. **Author contributions:** L.Z.: Writing—original draft, conceptualization, investigating, writing—review and editing, methodology, funding acquisition, validation, supervision, formal analysis, software, project administration, and visualization. T.L.D.: Conceptualization, writing—review and editing, and methodology. V.K.: Writing—review and editing, methodology, and data curation. A.R.: Writing—review and editing, methodology, data curation, and software. C.S.: Conceptualization, investigation, writing—review and editing, methodology, resources, funding acquisition, and software. X.Y.: Writing—review and editing, methodology, data curation, validation, and software. F.Z.: Methodology and data curation. A.W.: Writing—original draft, writing—review and editing, and methodology. J.Z.: Investigation, writing—review and editing, resources, and validation. Q.G.: Writing—review and editing. S.L.: Writing—review and editing. **Competing interests:** The authors declare that they have no competing interests. **Data and materials availability:** The gridded SSH dataset observed by satellite altimetry is available at the Copernicus Marine and Environment Monitoring Service center (https://data.marine.copernicus.eu/product/SEALEVEL_GLO_PHY_CLIMATE_L4_MY_008_057/services). The hourly water level time series at different TG stations are available from the NOAA's National Ocean Service (https://tidesandcurrents.noaa.gov/stations.html?type=Historic+Water+Levels). The vertical land movement rates are based on the Glacial Isostatic Adjustment model ICE-5G v1.3 distributed by the PSMSL (https://psmsl.org/train_and_info/geo_signals/gia/peltier/index.php). The NOAA's minor flood thresholds were documented in the NOAA technical report (https://oceanservice.noaa.gov/hazards/sealevelrise/sealevelrise-tech-report-sections.html). The data for the figures in this article are available online at https://doi.org/10.5281/zenodo.14833502. All data needed to evaluate the conclusions in the paper are present in the paper and/or the Supplementary Materials.

Submitted 13 August 2024
Accepted 10 April 2025
Published 16 May 2025
10.1126/sciadv.ads4419